



Cite this: *J. Mater. Chem. A*, 2022, **10**, 9137

## Comprehensive physicochemical and photovoltaic analysis of different Zn substitutes (Mn, Mg, Fe, Ni, Co, Ba, Sr) in CZTS-inspired thin film solar cells†

Stener Lie,<sup>ab</sup> Maxim Guc,<sup>id</sup> Venkatesh Tunuguntla,<sup>d</sup> Victor Izquierdo-Roca,<sup>id</sup> Susanne Siebentritt<sup>id</sup><sup>d</sup> and Lydia Helena Wong<sup>id</sup><sup>\*ab</sup>

The relatively stagnant efficiency of  $\text{Cu}_2\text{ZnSnS}_4$  (CZTS) kesterite thin film solar cells has led to the exploration of alternative materials based on the kesterite structure. The unavoidable formation of Cu-Zn disorder-related defects and Sn-related deep defects such as  $\text{Sn}_{\text{Zn}}$  and its cluster in CZTS prompt various attempts to substitute Zn. However, the underlying principles behind the selection of the cation substitutes remain unclear since most studies have been performed using different synthetic strategies. In this study, CXTS ( $X = \text{Zn, Mn, Mg, Ni, Fe, Co, Ba, Sr}$ ) thin films are synthesized by a facile spray pyrolysis and sulfurization method, and their physical properties and device performance are compared. It is found that a majority of the compounds form a tetragonal structure (kesterite or stannite); however, Mg + CTS and Ni + CTS are unstable in their quaternary structure and form a mixture of secondary phases, while CBaTS and CSrTS form trigonal structures. From UV-Vis spectroscopy, it is found that CMnTS, CBaTS and CSrTS exhibit steep and clear absorption edges, which make them promising solar cell absorbers. Meanwhile, high carrier concentrations ( $>10^{18} \text{ cm}^{-3}$ ) are observed for the compounds with transition metal substitutes (Mn, Mg, Ni, Fe, Co). Promising photovoltaic responses are observed in CMnTS, Mg + CTS, CBaTS and CSrTS, with CBaTS having the highest device performance possibly due to the lower band tailing, as observed from the photoluminescence and external quantum efficiency measurements. From these findings, correlations among the suitable cation substitutes for kesterite-inspired compounds are discussed and a guide for screening different cation substitutes for Zn in alternative I<sub>2</sub>-II-IV-VI<sub>4</sub> solar cells is provided.

Received 10th January 2022  
 Accepted 10th March 2022

DOI: 10.1039/d2ta00225f  
[rsc.li/materials-a](http://rsc.li/materials-a)

## 1. Introduction

$\text{Cu}_2\text{ZnSnS}_4$  (CZTS) is a promising candidate for low-cost and environmentally friendly thin-film solar cells, but its highest

recorded efficiency is 12.6% (ref. 2 and 3) (13% for certified active area measurement<sup>4</sup> and 13.5% with 5% Ag substitution<sup>5</sup>), which is still considerably lower than the theoretical Shockley-Queisser limit of 32.4% for CZTS.<sup>6</sup> Although notable progress has been made in achieving a CZTS solar cell with an efficiency of around 12%, especially using various solution process strategies,<sup>7-12</sup> the main issue originating from the high open circuit voltage ( $V_{\text{oc}}$ ) deficit still stands. Several previous studies have analyzed and reviewed the progress and performance limiting factors in kesterite.<sup>13-20</sup> In earlier studies,  $\text{Cu}_{\text{Zn}}$  antisite defects have been suggested as the main culprit for the  $V_{\text{oc}}$  deficit (including in high quality single crystal (CZTSSe)).<sup>21-28</sup> However, recent theoretical and experimental works have found that Sn-related defects might be more influential to the  $V_{\text{oc}}$  deficit problem.<sup>29-33</sup> Even though Sn can be replaced by other elements, there is a limited option for Sn replacement (mainly Ge).<sup>34-41</sup> Another alternative is to replace Zn, which forms the Sn-related deep defects  $\text{Sn}_{\text{Zn}}$ . Replacing Zn with Cd<sup>10,42-47</sup> has shown promising improvement, which is correlated to a decrease in  $\text{Cu}_{\text{Zn}}$  antisite defects and the suppression of deep defects, resulting in a better carrier lifetime, sharper absorption band edge and  $V_{\text{oc}}$  improvement. Unfortunately, Cd is not an ideal

<sup>a</sup>School of Materials Science & Engineering, Nanyang Technological University, 50 Nanyang Ave, 639798, Singapore. E-mail: [lydiawong@ntu.edu.sg](mailto:lydiawong@ntu.edu.sg)

<sup>b</sup>Singapore-HUJ Alliance for Research and Enterprise (SHARE), Nanomaterials for Energy and Energy-Water Nexus (NEW), Campus for Research Excellence and Technological Enterprise (CREATE), Singapore, 138602 Singapore

<sup>c</sup>Catalonia Institute for Energy Research (IREC), Jardins de les Dones de Negre, 1, 2<sup>a</sup> pl., 08930 Sant Adrià de Besòs, Barcelona, Spain

<sup>d</sup>Laboratory for Photovoltaics, University of Luxembourg, 42, rue du Brill, 4422 Belvaux, Luxembourg

† Electronic supplementary information (ESI) available: Plan-view SEM images of the CXTS films; grain size distribution for the CXTS thin films; local EDS measurement for CSrTS; XRD pattern of the CXTS films with each respective reference patterns; normalized XRD peaks for CXTS compounds at 27° to 30°; Raman spectra under 785 nm excitation wavelength; Raman scattering spectra of CXTS compounds with the dominant quaternary phase measured under 532 nm; Tau<sub>e</sub> plot based on UV-Vis spectroscopy; device parameters for non-stoichiometric CXTS; device parameters for stoichiometric CXTS; photoluminescence spectra of CZTS, CMnTS, Mg + CTS, CBaTS and CSrTS. See DOI: 10.1039/d2ta00225f



substitute due to its toxicity. There are several other possible Zn substitutes that satisfy the octet rule and are less toxic and more abundant. Table 1 lists all of the possible cations with the +2 oxidation state from different cation groups, such as alkaline earth metals, transition metals, post-transition metals, and rare-earth metals. From the list, seven cations can be considered suitable as environmentally friendly substitutes for Zn, such as Mn, Ni, Fe, Co, Mg, Sr, and Ba. All of these cations have +2 oxidation state as their stable states and have different cation radii with Zn/Cu in the 4-fold coordination.<sup>48,49</sup> Based on the abundance (atom fraction) of the chemical elements in Earth's upper continental crust data from the United States geological survey (USGS),<sup>50-52</sup> these elements are considered abundant (more than 10 atoms of element per 10<sup>6</sup> atoms of Si) and are not categorized as precious or rare-earth metals. According to the Agency for Toxic Substances and Disease Registry (ATSDR),<sup>53</sup> these elements have little to no health effect after low levels of exposure (except for Ba in certain soluble compounds). The last criterion is their stability as quaternary compounds, which have been reported by several theoretical calculation or experimental findings. Several quaternary compounds (*i.e.*, Cu<sub>2</sub>FeSnS<sub>4</sub> (CFTS),<sup>83,84</sup> Cu<sub>2</sub>MnSnS<sub>4</sub> (CMnTS),<sup>85-88</sup> Cu<sub>2</sub>SrSnS<sub>4</sub> (CSrTS) and Cu<sub>2</sub>BaSn(S,Se)<sub>4</sub> (CBaTS)<sup>65,66,89-92</sup> have shown promising photovoltaic performance. As the morphology and chemical composition of the kesterite-inspired compounds often depend on the synthesis approaches, it is hard to deduce a conclusive comparison and selection criteria based on the reported data,

which were synthesized and characterized using different approaches. Therefore, this study aims to comprehensively compare the cation substitute compounds based on the facile spray pyrolysis technique to fabricate CXTS (X = Mn, Mg, Ni, Fe, Co, Ba, Sr). The structural, phases, morphology and optoelectronic properties are correlated with the photovoltaic performances and their electronic configuration. Several design considerations were also drawn and summarized from this study, which may serve as a guide to designing alternative I<sub>2</sub>-II-IV-VI<sub>4</sub> absorbers.

## 2. Experimental section

### 2.1 Cu<sub>2</sub>XSnS<sub>4</sub> thin film preparation

The terms "Cu<sub>2</sub>XSnS<sub>4</sub>" (X = Zn, Mn, Mg, Ni, Fe, Co, Ba, Sr) in this study refer to the compounds based on the precursor solution, and do not reflect the final composition and phases in the films. The precursor solution was prepared by dissolving copper chloride dihydrate (CuCl<sub>2</sub>·2H<sub>2</sub>O, 0.072 M), tin chloride dihydrate (SnCl<sub>2</sub>·2H<sub>2</sub>O, 0.036 M) and thiourea (CH<sub>4</sub>N<sub>2</sub>S, 0.64 M) into 50 ml D.I. water. Following that, divalent cation (0.036 M) was added which either zinc chloride (ZnCl<sub>2</sub>), manganese chloride tetrahydrate (MnCl<sub>2</sub>·4H<sub>2</sub>O), magnesium chloride hexahydrate (MgCl<sub>2</sub>·6H<sub>2</sub>O), nickel chloride (NiCl<sub>2</sub>), iron(II) chloride (FeCl<sub>2</sub>), cobalt(II) chloride hexahydrate (CoCl<sub>2</sub>·6H<sub>2</sub>O), strontium chloride hexahydrate (SrCl<sub>2</sub>·6H<sub>2</sub>O) or barium chloride dihydrate (BaCl<sub>2</sub>·2H<sub>2</sub>O). The chemical precursors were

Table 1 List of possible cation substitutes for Zn in Cu<sub>2</sub>ZnSnS<sub>4</sub>

		Electronic configuration	Criteria			
Cations with +2 oxidation state			Earth-abundant <sup>50-52</sup>	Non-toxic <sup>53</sup>	Quaternary chalcogenide	Ref.
Alkaline earth metals (group IIA)	Beryllium (Be)	[He]2s <sup>2</sup>	✓	✗	✓ <sup>a</sup>	54 and 55
	Magnesium (Mg)	[Ne]3s <sup>2</sup>	✓	✓	✓	56-58
	Calcium (Ca)	[Ar]4s <sup>2</sup>	✓	✓	✗	56
	Strontium (Sr)	[Kr]5s <sup>2</sup>	✓	✓	✓	59-62
	Barium (Ba)	[Xe]6s <sup>2</sup>	✓	✓ <sup>b</sup>	✓	63-66
	Radium (Ra)	[Rn]7s <sup>2</sup>	✗	✗	✗	
Transition metals	Manganese (Mn)	[Ar]4s <sup>2</sup> 3d <sup>5</sup>	✓	✓	✓	67-70
	Iron (Fe)	[Ar]4s <sup>2</sup> 3d <sup>6</sup>	✓	✓	✓	71-73
	Cobalt (Co)	[Ar]4s <sup>2</sup> 3d <sup>7</sup>	✓	✓ <sup>c</sup>	✓	73-76
	Nickel (Ni)	[Ar]4s <sup>2</sup> 3d <sup>8</sup>	✓	✓ <sup>c</sup>	✓	77 and 78
	Copper (Cu)	[Ar]4s <sup>1</sup> 3d <sup>10</sup>	✓	✓	✓(as Cu <sup>+</sup> )	
	Zinc (Zn)	[Ar]4s <sup>2</sup> 3d <sup>10</sup>	✓	✓	✓	
	Palladium (Pd)	[Kr]4d <sup>10</sup>	✗	✓	✗	
	Cadmium (Cd)	[Kr]5s <sup>2</sup> 4d <sup>10</sup>	✗	✗	✓	79-81
	Platinum (Pt)	[Xe]6s <sup>1</sup> 4f <sup>14</sup> 5d <sup>9</sup>	✗	✓	✗	
	Mercury (Hg)	[Xe]6s <sup>2</sup> 4f <sup>14</sup> 5d <sup>10</sup>	✗	✗	✗	
	Copernicium (Cn)	[Rn]7s <sup>2</sup> 5f <sup>14</sup> 6d <sup>10</sup>	✗	✗	✗	
	Germanium (Ge)	[Ar]4s <sup>2</sup> 3d <sup>10</sup> 4p <sup>2</sup>	✗	✓	✓(as Ge <sup>4+</sup> )	61, 68 and 82
	Tin (Sn)	[Kr]5s <sup>2</sup> 4d <sup>10</sup> 5p <sup>2</sup>	✓	✓	✓(as Sn <sup>4+</sup> )	
Post-transition metals	Lead (Pb)	[Xe]6s <sup>2</sup> 4f <sup>14</sup> 5d <sup>10</sup> 6p <sup>2</sup>	✓	✗	✗	
	Polonium (Po)	[Xe]6s <sup>2</sup> 4f <sup>14</sup> 5d <sup>10</sup> 6p <sup>4</sup>	✗	✗	✗	
	Europium (Eu)	[Xe]6s <sup>2</sup> 4f <sup>7</sup>	✗	✓	✗	
	Nobelium (No)	[Rn]7s <sup>2</sup> 5f <sup>14</sup>	✗	✗	✗	
Lanthanide						
Actinides						

<sup>a</sup> Metastable. <sup>b</sup> Toxic as soluble compounds. <sup>c</sup> May induce a health hazard.



purchased from Sigma Aldrich with a purity of 99.99%. There are two types of precursors made, the stoichiometric and non-stoichiometric ratios. Deviations in the non-stoichiometric ratio had Cu-poor ( $\text{Cu}/(\text{Zn} + \text{Sn}) = 0.75$ ) and X-rich ( $\text{X}/\text{Sn} = 1.2$ ) composition. The stoichiometric samples were used to perform the thin film characterizations, while the non-stoichiometry samples were focused on the device analysis. Dilute HCl (0.1 mol) was added to adjust the pH value to 2. It is to ensure solution stability specially to prevent  $\text{SnO}_2$  precipitation during the spraying process.<sup>93,94</sup> Mo-coated glass substrates were cleaned using Alconox® detergent, ethanol, isopropyl alcohol (IPA) and D.I. water in an ultrasonic bath. The precursor was sprayed on substrates, which were heated. The hot plate temperature ( $450\text{ }^\circ\text{C} = 280\text{ }^\circ\text{C}$  substrate temperature), gas pressure ( $\sim 20$  psi), and solution flow rate ( $1.6\text{ ml min}^{-1}$ ) were the spray parameters used to obtain the  $1\text{ }\mu\text{m}$  thin film. The as-deposited films were sulfurized at  $600\text{ }^\circ\text{C}$  for 40 min in a two-zone tube furnace. The sulfur source (300 mg) in another zone of the furnace was heated at lower temperature ( $200\text{ }^\circ\text{C}$ ). The tube was filled with Ar gas ( $\sim 300$  mBar).

### 2.3 $\text{Cu}_2\text{SnS}_4$ device fabrication

The solar cell devices were fabricated with a Mo/CXTS/CdS/ITO/Ag-paste configuration. Chemical bath deposition (CBD) of the CdS buffer layer was operated at  $80\text{ }^\circ\text{C}$  for 8 min.  $\text{Cd}(\text{SO}_4)$  (0.015 M),  $\text{CH}_4\text{N}_2\text{S}$  (0.75 M) and  $\text{NH}_4\text{OH}$  (28–30%) were used to fabricate the CdS. Following that, the Sn:InO (ITO) window layers were sputtered on top of CdS with a thickness of around 100–200 nm. The devices were subjected to post-annealing treatment at  $300\text{ }^\circ\text{C}$  for 10 min in an Ar atmosphere ( $\sim 300$  mBar). After that, the samples were manually scribed to make a grid with each square having an area of  $0.16\text{ cm}^2$  (active area of  $0.15\text{ cm}^2$ ). Finally, the Ag paste was put on top to act as an electrode.

### 2.4 Thin films and device characterizations

Scanning electron microscopy (SEM) and energy dispersive X-ray spectroscopy (EDS) characterizations were performed by FESEM (FESEM, JOEL, JSM-7600F). X-ray diffraction (XRD) patterns were collected by Bruker D8 Advance with  $\text{Cu K}\alpha$  ( $1.5406\text{ \AA}$ ) as the XRD source. Raman scattering spectra were measured in a backscattering configuration using Horiba Jobin-Yvon FHR-640 and Horiba Jobin-Yvon iHR-320 monochromators, both coupled with CCD detectors. The former monochromator was used together with a solid-state YAG:Nd (532 nm) laser as the excitation sources. The iHR-320 monochromator was optimized to the NIR range, and was used with a 785 nm diode laser. All spectra were normalized to the position of the main peak of monocrystalline Si at  $520\text{ cm}^{-1}$ . Absorption properties of the films were conducted on a Shimadzu UV-3600 apparatus with a scanning range from 400 nm to 1400 nm. An in-house built set-up was used for all of the calibrated photoluminescence measurements. For excitation, monochromatic lights of diode lasers (405 and 663 nm) were used. The beam diameter was measured with a CCD-camera, and the Gaussian spot size radius of 1.33 mm was used for

probing the samples. The photon flux was set to between  $1.7 \times 10^{17}$  to  $0.9 \times 10^{17}$  photons  $\text{cm}^{-2}\text{ s}^{-1}$ , which is equivalent to the flux of an AM1.5 sun spectrum of 1.4 to 2 eV, respectively. For the intensity correction, the laser power was calibrated with a power meter. Hall measurements were performed on exfoliated samples (exfoliated from Mo to quartz substrate) in the parallel dipole line AC Hall setup.<sup>95,96</sup> Device characterization, such as current density–voltage ( $J$ – $V$ ) and external quantum efficiency (EQE), were performed in a Xe-based solar simulator with Keithley 2612A and PVE300 from Bentham, respectively.

## 3. Results and discussions

### 3.1 Morphology and chemical composition of CXTS

Fig. 1 shows the cross-section SEM images of the CXTS thin films. CZTS and CMnTS have similar morphology, forming a dense film made of mostly grains equivalent to their thickness. Meanwhile, Mg + CTS and Ni + CTS films consist of small grains with an evident layered structure for Mg + CTS. CCoTS and CFeTS films exhibit a dense film with a mixture of large and small grains. In addition, the adhesion between the films and Mo substrate are poor as observed from the voids in the interface. Lastly, CBaTS and CSrTS exhibit the largest average grain sizes (Fig. S1†) compared to the other cations, even though the large grains in CSrTS are not uniformly distributed (Fig. S2†). This result is consistent with the EDS measurement, as shown in Table 2. Based on the standard deviations of elemental compositions, most of the films show lateral uniformity and homogenous chemical composition, except for Mg + CTS and CSrTS. These two compounds showed higher standard deviation than the other substitutes, which could be related to the distinct layered and non-uniform morphology in Mg + CTS and CSrTS, respectively. Further examination of CSrTS by EDS revealed that the large grain phase belongs to the CSrTS quaternary phase. Meanwhile, the small grains did not contain Sr (Fig. S3†), thus indicating the formation of binary or ternary secondary phases consisting of only Cu–Sn–S. These small grains were also observed in Mg + CTS and Ni + CTS, which might also be attributed to the formation of similar secondary phases. Deviations from the initial stoichiometric composition of the precursor were observed in all compounds to various extents, as seen from the cations' ratio. This phenomenon is commonly found during the formation of quaternary compounds. It is related to the high synthesis temperature and low partial pressure of binary sulfides, which results in cation loss, as reported in the case of CZTS.<sup>97</sup> Further optimization on the sulfurization process for each compound needs to be done to have better control of the layer's composition.

### 3.2 Crystal structure and phase analysis of the CXTS thin films

Fig. 2 exhibits the XRD pattern and Raman scattering spectra of the CXTS films. The Bragg reflections at  $2\theta = 40.5^\circ$ , which corresponds to Mo substrate, are evident in all samples. The XRD data from the CXTS films exhibit two distinct characteristics, which can be classified into two groups of crystal system. The lower number of diffraction planes in CZTS, CMnTS, Mg +



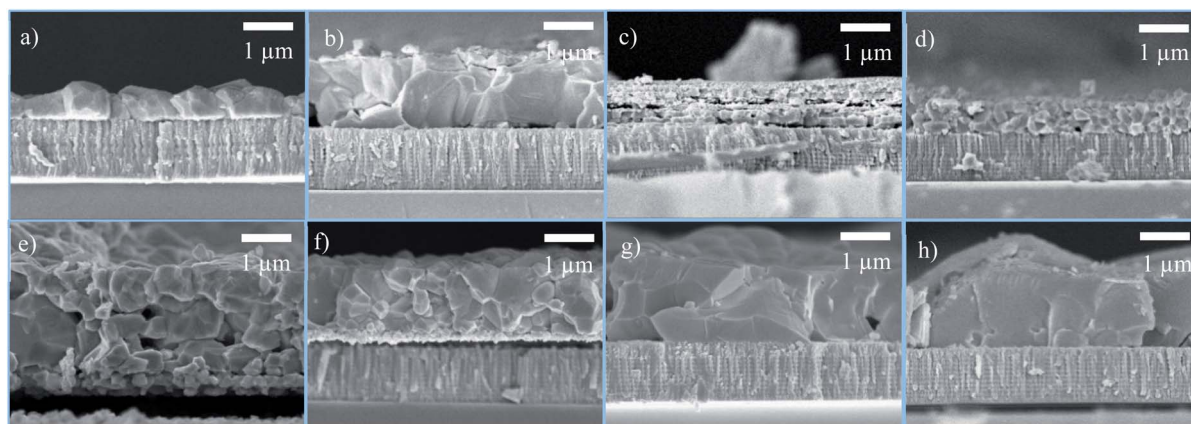


Fig. 1 Cross-sectional SEM images of the CXTS films: (a) CZTS, (b) CMnTS, (c) Mg + CTS, (d) Ni + CTS, (e) CFeTS, (f) CCoTS, (g) CBaTS and (h) CSrTS.

Table 2 Elemental composition of CXTS from energy dispersive spectroscopy measurements<sup>a</sup>

	Elemental composition (at%)				Elemental ratios		
	Cu	X	Sn	S	Cu/(X + Sn)	(X)/Sn	(Cu + X + Sn)/S
CZTS	23.2 ± 0.1	11.6 ± 0.2	13.8 ± 0.5	51.4 ± 0.6	0.91	0.84	0.94
CMnTS	23.1 ± 0.6	11.4 ± 0.2	12.5 ± 0.4	53.0 ± 1.0	0.97	0.91	0.89
CFeTS	25.1 ± 0.5	12.2 ± 0.3	12.5 ± 0.3	50.1 ± 0.6	1.02	0.97	0.99
CCoTS	24.8 ± 0.4	10.2 ± 0.2	13.2 ± 0.1	51.8 ± 0.4	1.06	0.78	0.93
CBaTS	24.1 ± 0.1	13.0 ± 0.2	11.2 ± 0.4	51.7 ± 0.2	0.99	1.17	0.93
CSrTS	20.0 ± 5.8	12.7 ± 5.0	15.6 ± 1.1	52.5 ± 2.1	0.76	0.88	0.91
Mg + CTS	20.8 ± 0.6	14.8 ± 2.4	11.5 ± 0.3	52.9 ± 1.6	0.80	1.29	0.89
Ni + CTS	22.8 ± 0.7	11.7 ± 0.4	14.0 ± 0.5	51.5 ± 0.3	0.89	0.84	0.94

<sup>a</sup> The elemental composition is calculated as an average of five different sampling areas from the plane-view SEM after sulfurization, and the error is the standard deviation. Elemental ratios are based on the average values elemental composition.

CTS, Ni + CTS, CFeTS and CCoTS indicates a higher symmetry system. These films exhibit similar strong diffraction peaks (reflections around 28° and 48°), which is common for crystal system compounds derived from a zinc blended structure, including ZnS and Cu<sub>2</sub>SnS<sub>3</sub>.<sup>98–100</sup> Meanwhile, the higher number of diffraction planes in CBaTS and CSrTS indicates a lower symmetry system. All of the analyzed thin films can be categorized into the tetragonal group for the higher symmetry system, and the trigonal group for the lower symmetry system. These categorizations are based on the identification of their individual diffractograms with reference diffractograms and theoretical predictions.<sup>54,56,61,62,101</sup>

An individual investigation was conducted on each film from the tetragonal group (Fig. S4†). The CZTS, CMnTS, CFeTS and CCoTS peaks correspond to their respective tetragonal peaks in the database (JCPDS 026-0575 for CZTS, JCPDS 051-0757 for CMnTS, JCPDS 044-1476 for CFeTS and JCPDS 026-0513 for CCoTS).<sup>102,103</sup> A systematic peak shift from the smallest cation (Co) to the largest (Mn) are observed, indicating lattice expansion due to the different ionic sizes (Fig. S5†). A peak shift is commonly found in the substitution study due to the lattice strain introduced by elements with different ionic sizes.<sup>104–106</sup> The main peaks

of Ni + CTS correspond to its quaternary compound (JCPDS 026-0552) with an obvious presence of the NiS<sub>2</sub> phase (grey circles).<sup>107</sup>

To further identify and confirm the formation of the quaternary and/or secondary phases, all of the stoichiometric thin films were also examined by Raman spectroscopy. Fig. 2b shows the average spectra measured in different points of the thin films under 532 nm excitation wavelength, and similar spectra measured under 785 nm are presented in Fig. S6.† Analysis of the obtained Raman spectra and comparison with the previously published results<sup>21,76,86,108–113</sup> allowed us to conclude that for most of the analyzed compounds, the quaternary phase is the dominant one. Furthermore, there was no or only a residual amount of the secondary phases present in the thin films. This is expected of the Mg + CTS and Ni + CTS compounds, for which the Raman scattering analysis exhibits only the mixture of ternary and binary secondary phases,<sup>1,107</sup> in accordance with the XRD results.

The general shape of the obtained Raman spectra of all analyzed compounds allowed for a conclusion about the common characteristic features for the quaternaries. Independent of the crystalline structure, the spectra were characterized by one intense peak (its position is indicated in the brackets



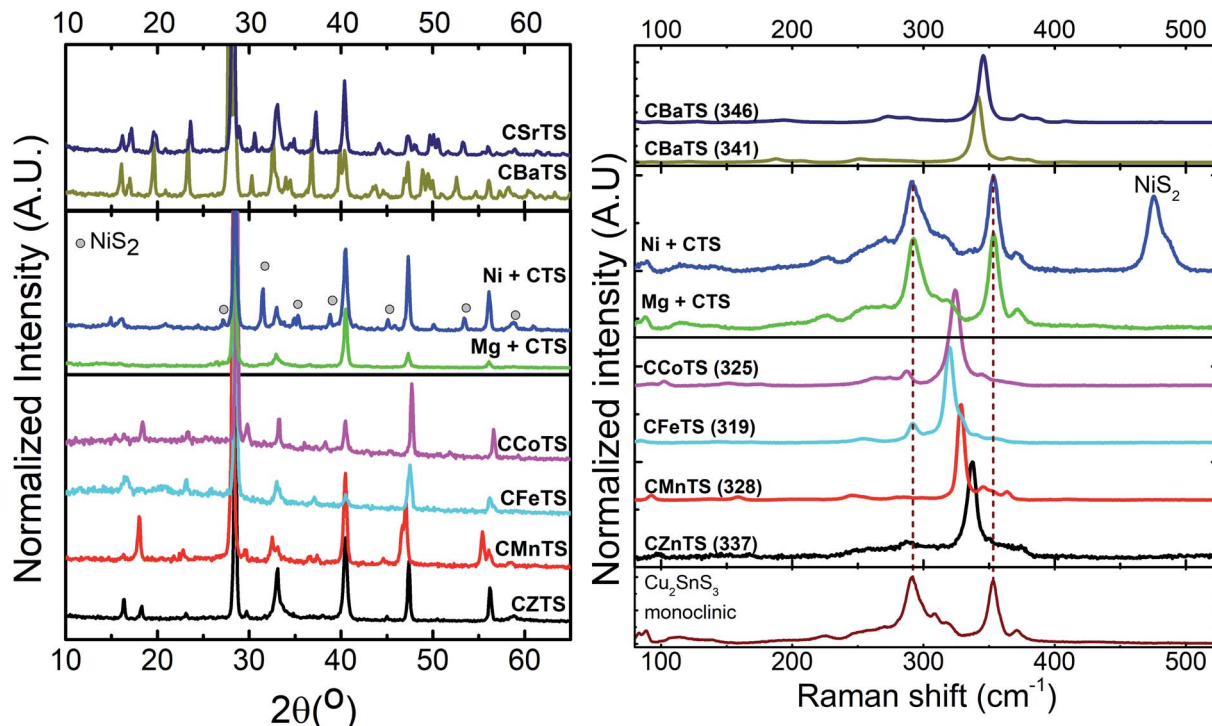


Fig. 2 X-ray diffraction patterns (left) and Raman scattering spectra measured under 532 nm excitation wavelength (right) for the CXTS films. Numbers indicate the position of the most intense Raman peak of the quaternary phase. The reference Raman spectra of monoclinic  $\text{Cu}_2\text{SnS}_3$  is added for convenience.<sup>1</sup>

close to each compound in the left panel of Fig. 2) and a series of peaks with lower intensity. In accordance with the previous analysis in the case of the quaternary compounds crystallized with a tetragonal Bravais lattice (CZTS, CMnTS, CFeTS and CCoTS), the most intense Raman peak is assigned to the anion vibrations.<sup>21,108,110,111,113</sup> This suggests an insignificant influence of the changes in the cation sub-lattice to the position of the main Raman peak, which is in line with the presented results. Slightly higher changes are expected in the peaks with lower intensity, and the main ones can be seen in the range of 240–300  $\text{cm}^{-1}$  (see Fig. S7†). Nevertheless, the general shape of the spectra of the tetragonal quaternary compounds is quite similar even for the low intensity peaks, as seen from Fig. S7.† This, however, is not true for the two compounds crystallized with the trigonal lattice (CBaTS and CSrTS). The lower symmetry of these two compounds also results in a higher amount of expected Raman peaks (up to 138 peaks can be seen in the Raman spectra, taking into account the LO/TO splitting and the irreducible representation for the space group  $P3_1$ ).<sup>114</sup> As a result, the general redistribution and the appearance of the peaks with low intensity for the trigonal compounds are significantly different from those of the tetragonal compounds. However, a notable similarity can be found between the Raman spectra of CBaTS and CSrTS with only a small blue shift of the peaks of the latter, which is in accordance with the smaller size of the Sr cation and expected shorter interatomic bounds.

Several remarks can be deducted from these quaternary compound formations. In this study, Mg + CTS and Ni + CTS do

not form a stable quaternary phase, while CBaTS and CSrTS form a trigonal shape instead of tetragonal. First, the unsuccessful fabrication of Mg + CTS seems to be related to the lack of a d-orbital in Mg. Although the d-orbital of Zn does not play an important role in the conduction and valence band edge formation in CZTS, it still contributes to the density of states formation.<sup>115</sup> A similar case for the remaining cations in this study (Fe, Co, Mn, Ba and Sr), their d-orbital also contributes to the density of states formation of CFeTS, CCoTS, CMnTS, CBaTS and CSrTS.<sup>54,61,64,116,117</sup> Even in CMnTS, the Mn d-orbital plays a more important role as it hybridizes with the s and p-orbitals to form a conduction band minimum (CBM).<sup>118</sup> Second, in the case of the Ni + CTS formation, there is a high similarity between its secondary phase and quaternary phase structure, which tends to make the phase separation easily occur. Ni + CTS has been shown (theoretically and experimentally) to have a stable quaternary  $P42c$  polytype cubic phase, which has a similar cubic phase with its secondary phase  $\text{NiS}_2$ .<sup>73,78,119–122</sup> Thus, it may be more difficult to obtain the quaternary compound and reaction kinetics during the growth of Ni + CTS must be carefully controlled to obtain a pure quaternary compound.<sup>123</sup> In addition, Ni has the smallest ionic radius in 4-fold coordination among the transition metal substitutes, which can increase the likelihood of Ni leaving the lattice.<sup>49</sup> Lastly, as observed in CBaTS and CSrTS, it emphasizes the importance of the ionic radius difference between the substitute and the other host cations (Cu and Sn in this study). If the ionic size difference is too large, a different structure will be formed.



### 3.3 Optoelectronic properties of the CXTS thin films

Fig. 3 shows the absorption spectra for the CXTS samples by UV-Vis spectroscopy. The spectra of the samples are classified into 4 figures based on the similarity in the absorption spectra shape, *i.e.*, CZTS and CMnTS, Mg + CTS and Ni + CTS, CFeTS and CCoTS, CBaTS and CSrTS. The partially filled orbital configuration of CFeTS and CCoTS might have different absorption profiles compared to the half-filled orbital CMnTS and fully-filled orbital CZTS.<sup>124</sup> Meanwhile, Mg + CTS and Ni + CTS are similar as they possess multiple absorption edges, which correspond to multiple band gaps due to the formed mixture of the secondary phases, including the formation of different polymorphs of the Cu-Sn-S system.<sup>1,98</sup> CBaTS and CSrTS have absorption edges at low wavelength. However, CSrTS exhibits a prominent low band gap absorption, which can be attributed to the small grains of the Cu<sub>2</sub>SnS<sub>3</sub> phase found in the EDS analysis. CZTS, CMnTS, CBaTS and CSrTS show steep absorption edges, while the rest have more gradual absorption edges.

From the absorption curve, the band gaps of these films were extracted based on Tauc plot (Fig. S8†)<sup>125</sup> and are tabulated in Table 3. The band gaps of CZTS, CMnTS, CFeTS, CSrTS and CBaTS are comparable with the previous findings.<sup>60,62,66,87,126–129</sup> However, the CSrTS sample also exhibits two smaller inflection points, which can be attributed to the band gap of the Cu<sub>2</sub>SnS<sub>3</sub> secondary phase (~0.92–0.95 eV).<sup>1,130</sup> In Mg + CTS and Ni + CTS, these correspond to the ternary phases' band gaps, orthorhombic Cu<sub>3</sub>SnS<sub>4</sub> (1.57 eV)<sup>130</sup> and monoclinic Cu<sub>2</sub>SnS<sub>3</sub> (1.10 and ~1.00 eV).<sup>1,130</sup> As for CCoTS, the band gap is estimated to be at a relatively smaller value than the reported values around 1.4–1.6 eV,<sup>75,76,131</sup> which might be due to severe band tailing for CCoTS in this study.

In terms of the electronic properties, all films possess p-type conductivity based on the Hall measurement. The carrier concentration and mobility of these films are tabulated in Table 3. In terms of the carrier concentration, CZTS and CBaTS have similar values around  $10^{15} \text{ cm}^{-3}$ , which is suitable for the solar cell material.<sup>132</sup> However, the carrier concentration of the other films are  $>10^{18} \text{ cm}^{-3}$ , which have been shown to possess poor photovoltaic performances.<sup>86,133</sup> The high concentration for Mg + CTS, Ni + CTS and CSrTS may be attributed to the Cu<sub>2</sub>SnS<sub>3</sub> secondary phase.<sup>98</sup> In terms of mobility, all of the films have mobility around  $0.5\text{–}2.7 \text{ cm}^2 \text{ V}^{-1} \text{ s}^{-1}$ , where CBaTS and CSrTS have the highest mobility.

The transition metal candidates (Fe, Ni, Co and Mn) exhibit high carrier concentration, which seems to be related to their multivalent properties. All of these metals possess multiple oxidation states due to their partially filled d-orbitals. Mn is expected to be more stable as the only one with half-filled 3d<sup>5</sup>-orbitals,<sup>134</sup> while the rest of the substitutes possess a partially filled orbital.<sup>135</sup> The compound could even be more stable and show potential in suppressing defects if the elemental substitute has a fully filled orbital as observed in Cd.<sup>44,46,47</sup> The unpaired electrons in the partially filled orbital contributes to the high carrier concentration either as a free electron or in traps. As for CBaTS and CSrTS, the different crystal structures result in a higher band gap and lower carrier concentration. However, the conducting secondary phase for CSrTS in this study increases the carrier concentration significantly.

### 3.4 Device characterization and analysis of the CXTS solar cells

Following the thin film studies, solar cell devices (Mo/CXTS/CdS/i-ZnO/ITO/Ag-paste) were fabricated and measured to

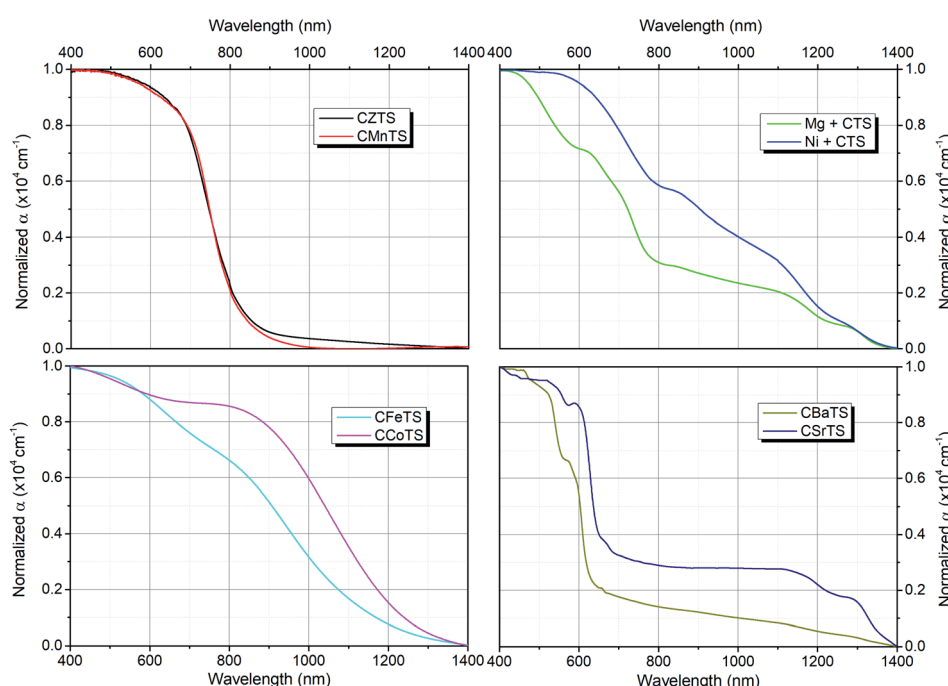


Fig. 3 Normalized absorption spectra for the CXTS films.



Table 3 Summary of the CXTS thin film characterization

Sample	Structure	Secondary phases	Band gap (eV)	Morphology	Hole concentration ( $\text{cm}^{-3}$ )	Hole mobility ( $\text{cm}^2 \text{V}^{-1} \text{s}^{-1}$ )
CZTS	Tetragonal (kesterite) $\bar{I}\bar{4}$	$\text{Cu}_3\text{SnS}_4$	1.60	Grain size $\approx$ thickness	$2.55 \times 10^{15}$	0.923
CMnTS	Tetragonal (stannite) $\bar{I}\bar{4}2\text{m}$	$\text{SnS}_x, \text{Mn-S}$	1.60	Grain size $\approx$ thickness	$2.56 \times 10^{19}$	0.501
CFeTS	Tetragonal (stannite) $\bar{I}\bar{4}2m$	—	1.20	Poor adhesion with Mo ( $\text{MoS}_2$ )	$1.91 \times 10^{19}$	1.107
CCoTS	Tetragonal (stannite) $\bar{I}\bar{4}2m$	—	1.10	Poor adhesion with Mo ( $\text{MoS}_2$ )	$2.95 \times 10^{21}$	0.466
CBaTS	Trigonal $P3_1$	—	2.00	Large grains, grain size $\approx$ thickness	$6.83 \times 10^{15}$	2.134
CSrTS	Trigonal $P3_221$	Cu-Sn-S phases	1.88	Large grains, non-uniform	$2.14 \times 10^{18}$	2.762
Mg + CTS	—	Orthorhombic $\text{Cu}_3\text{SnS}_4$ , monoclinic $\text{Cu}_2\text{SnS}_3$	1.57	Small grains, non-uniform (layered)	$2.92 \times 10^{18}$	1.083
Ni + CTS	—	$\text{NiS}_2$ (cubic), monoclinic $\text{Cu}_2\text{SnS}_3$	1.10	Small grains	$1.97 \times 10^{19}$	1.579

further understand the effect of different cations on the photovoltaic performance. The devices were fabricated under several different conditions, such as stoichiometric and non-stoichiometric ratios (Cu-poor, X-rich), without post-annealing and post-ITO deposition annealing. The non-stoichiometric ratio and post-annealing after ITO depositions are a commonly reported strategy in boosting the CZTS performance.<sup>93,136–139</sup> Fig. S9† shows the statistical solar cell parameters of the non-stoichiometric (Cu-poor and X-rich) CXTS devices with and without post annealing. The non-filled and striped box represent solar cell devices without and with post-device annealing, respectively.

The CXTS devices with the non-stoichiometric condition perform better than the stoichiometric one, especially  $V_{\text{oc}}$  (Fig. S10†). CMnTS, Mg + CTS, CBaTS and CSrTS show noticeable photovoltaic responses. On the other hand, devices with and without post annealing show that Ni + CTS, CFeTS and CCoTS does not produce photovoltaic response, even though some literature reported photovoltaic response for these three compounds.<sup>77,83,140,141</sup> This finding is also in line with the absorption edges gradient of the thin films where the four substitutes with steep slope show photovoltaic performance. Several reasons can be attributed to this finding. First, the Ni + CTS quaternary compound does not seem to form and there are prominent  $\text{NiS}_2$  secondary phases in this study. Second, the morphologies of CFeTS and CCoTS suffer from the poor adhesion with Mo, which creates an issue for the photovoltaic device. Lastly, in the reported literature, the evident photovoltaic performances for these three compounds are observed in different device architectures, such as using different buffer layers ( $\text{Bi}_2\text{S}_3$  for CFeTS<sup>83</sup>) and in a sensitized solar cell structure ( $\text{ZnO}/\text{ZnS}$  nanorods<sup>141</sup>). The post-device annealing also exhibits improvement for all films, except for CBaTS. Redistributions of the cations and anions were commonly observed as the effect of these post-device annealing events. As CBaTS does not seem to suffer from a disordered structure like kesterite CZTS,<sup>61,142</sup> it is possible that the post-device annealing disrupts the structure, instead of improving it.

The  $J-V$  characteristics of the respective CXTS “champion” cells after annealing under one sun illumination is shown in

Fig. 4a. Ni + CTS, CFeTS and CCoTS displayed an ohmic response, which illustrates the non-diode response from these materials. Among these cells, CZTS as a reference performs the best with an efficiency of 5.66%. CBaTS exhibits the second best performing cells, and is the best among the substitutes with an efficiency of 1.06%. The low  $J_{\text{sc}}$  for CBaTS is expected due to its high band gap, but the  $V_{\text{oc}}$  is quite low with respect to the band gap. In comparison with the literature, the highest efficiency CBaTS is achieved at 1.7% with  $V_{\text{oc}}$  being  $\sim 0.2$  V higher than in this study.<sup>66</sup> The  $V_{\text{oc}}$  deficit might be due to the unoptimized cation ratio, deposition parameters or buffer layer (Cds might not have the best band alignment) and possible secondary phase. Nevertheless, this result is comparable with the highest reported, and further optimization is expected to improve the performance. The efficiency of CMnTS ( $\eta = 0.56\%$ ) is also not far behind the record in the literature ( $\eta = 0.91\%$ ).<sup>87</sup> In fact, the  $V_{\text{oc}}$  and fill factor in this study is slightly higher than the record, while the decreased efficiency is governed by the lower  $J_{\text{sc}}$ , which can be improved by thickness optimization. It should be noted that the photovoltaic responses of Mg + CTS and CSrTS are most likely attributed to the CTS secondary phases. In general, the poor performances for some of these devices can be attributed to the suboptimal morphology, high carrier concentration, low mobility and secondary phases of the films.

To further understand the charge collection of these films, external quantum efficiency measurements were performed on the CXTS devices. From Fig. 4b, only CZTS, CMnTS, Mg + CTS, CBaTS and CSrTS show quantum efficiency signals, which is consistent with the photovoltaic response. A similar trend with their respective photovoltaic performances is also observed. The EQEs of Mg + CTS and CSrTS show extended gradual decreasing slopes, indicating the presence of low band gap CTS secondary phases. The sharp drop around 600 nm for CBaTS indicates low band fluctuation and tailing, which is an issue in CZTS,<sup>143,144</sup> while its relatively high band gap makes this compound promising for the semitransparent and tandem applications.

A photoluminescence study was also performed on the five samples, which exhibited the photovoltaic response (Fig. S11†). Table 4 tabulates the extracted parameters from the PL response, details on the parameter extraction can be found in



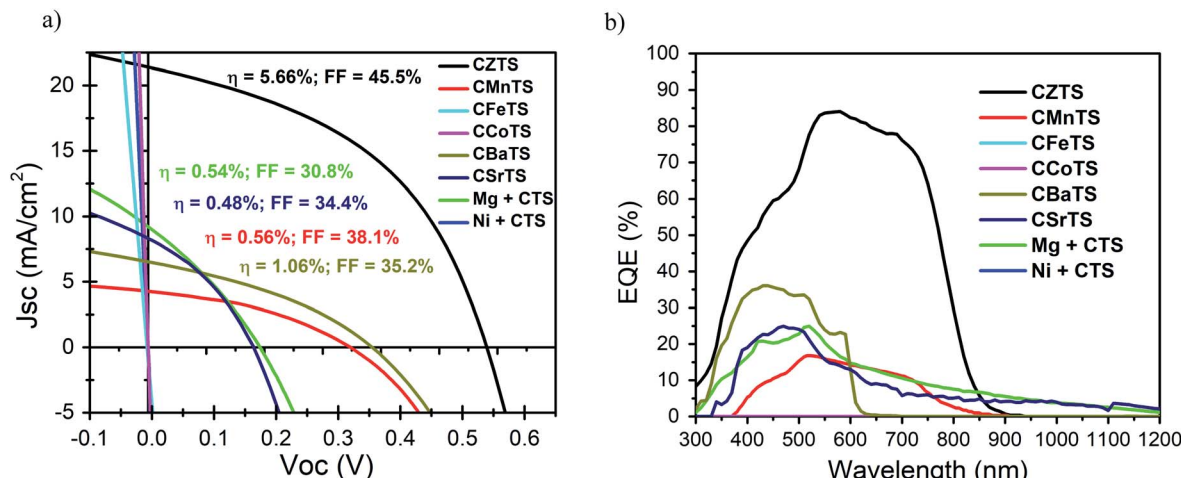


Fig. 4 (a)  $J$ – $V$  curve for the "champion" cell from each of the CXTS films. (b) External quantum efficiency for the CXTS solar cells with their respective extracted band gap and  $J_{sc}$ . Each CXTS film (represented by different colors) has two EQE responses; the solid line represents the post annealed film response and dashed line represents the response for the film without post annealing.

a previous study.<sup>145</sup> All of the measurements were performed at room temperature, and were spectrally corrected by using a commercially calibrated halogen lamp with a known spectrum and absolutely calibrated with the help of a power meter. All of the absorbers were passivated with 50 nm of the CdS layer by chemical bath deposition. The PL measurements, except for Sr and Ba substituted CXTS samples, were carried out at room temperature with a 663 nm wavelength diode laser as the excitation source. Since the band gaps of the Sr and Ba-substituted CXTS samples are relatively higher, a blue laser (405 nm) was used as the excitation source. Although the excitation wavelength of the laser is higher than the bandgap of CdS, the CdS thickness is negligible, and the absorption of the passivated layer is nearly negligible in the band gap region of the absorber. The external radiative efficiency (ERE) deduced from the calibrated PL spectrum was then used to determine the QFLS,

$$QFLS = V_{oc}^{SQ} + (KT/q)\ln(ERE)$$

where  $ERE = \frac{\text{photons emitted by absorber}}{\text{incident photons}}$  and  $V_{oc}^{SQ} = 0.93(E_{PL}/q) - 0.176 \text{ V}$ .<sup>145</sup>

CZTS and CMnTS exhibit well defined single peaks in their PL spectra (1.26 and 1.357 eV, respectively), with the  $E_{PL}$  value

closer to their respective  $E_g$ . This indicates that the PL response is dominated by the quaternary compounds without significant secondary phase contributions in comparison with the other compounds. The significant differences between the  $E_g$  and  $E_{PL}$  in these two compounds highlight the poor performances due to recombination losses. The  $E_{PL}$ , which are less than  $E_g$ , may indicate radiative recombination *via* deep tail states (band-tail to band-tail recombination).<sup>146</sup> It is also possible that the free-to-bound transition occurs due to the acceptor state recombination.<sup>147</sup> In conjunction with the low mobility, these findings also imply the lower carrier lifetime issue. Meanwhile, the spectral responses of the Mg + CTS, CBaTS and CSrTS films seem to be dominated by their secondary phases or deep defects (Fig. S11†), which explains the very high carrier concentration and poor performances of these devices. Mg + CTS, which forms a lower bandgap Cu–Sn–S secondary phase in this study, shows  $E_{PL}$  around the band gap of Cu–Sn–S. As for CBaTS and CSrTS, the PL peak from their respective quaternary compounds was found to be very close to their  $E_g$  at the high energy level. However, there are other more dominant broad peaks at lower energy levels. These can be related to the secondary phases with a lower band gap or deep defects in these structures, which is often found to generate high density of bulk recombination

Table 4 Extracted parameters from the photoluminescence for the samples with a photovoltaic response<sup>a</sup>

	$E_g$ (eV)	ERE (%)	$E_{PL}$ (eV)	$V_{oc}[\text{SQ}]$ (eV)	QFLS (eV)	QFLS loss (eV)	$V_{oc}$ (eV)	QFLS- $V_{oc}$ (eV)
CZTS	1.6	$1.904 \times 10^{-4}$	1.260	0.996	0.667	0.329	0.581	0.086
CMnTS	1.6	$2.697 \times 10^{-5}$	1.357	1.085	0.707	0.378	0.345	0.362
CBaTS	2	$7.74 \times 10^{-3}$	1.133	0.878	0.641	0.237	0.380	0.261
CSrTS	0.92, 0.95, 1.88	$2.74 \times 10^{-3}$	1.155	0.898	0.635	0.263	0.181	0.454
Mg + CTS	1, 1.1, 1.57	$3.920 \times 10^{-5}$	0.920	0.678	0.310	0.368	0.191	0.119

<sup>a</sup> ERE = external radiative efficiency,  $E_g$  = band gap from UV-Vis,  $E_{PL}$  = photoluminescence peak,  $V_{oc}[\text{SQ}]$  =  $V_{oc}$  based on the Shockley Quissler limit from the  $E_{PL}$ , QFLS = quasi Fermi level splitting.



centers.<sup>89</sup> The ERE and QFLS loss in CBaTS and CSrTS are more promising than CZTS. The ERE is defined as a ratio between the emitted photon flux and excitation flux, which means that the quality of the radiative emission in these two films seems to be better than CZTS in this study.<sup>148</sup> The QFLS loss is quantified as the difference between the  $V_{oc}$ [SQ] and the QFLS. This can be related to the non-radiative recombination quality of the film,<sup>149</sup> which shows that CBaTS and CSrTS have fewer non-radiation recombinations than the other films. The last parameter is the difference between QFLS and the devices'  $V_{oc}$ , which can indicate the recombination at the interface.<sup>150,151</sup> The results show that the four cation substitutes showing photovoltaic responses have more detrimental interface properties than CZTS. This indicates the need for alternative buffer layers, as some of these compounds have a larger band gap than CZTS, which makes CdS an unsuitable choice. Interface treatment might also be required to improve the device performance of these films. A previous study reported that the combination of CBaTS or CSrTS with a CdS buffer layer is not optimal because the conduction bands of CBTS and CSTS lie at significantly higher energy levels than in CIGS and CZTS. Therefore, although CBaTS and CSrTS are promising alternatives due to less recombination near the band edge based on PL and EQE, the deep defects and interface recombination require further optimization and alternative device structure to achieve good power conversion efficiency.

## 4. Conclusion

In summary, investigation on the effect of different cation substitutes for Zn in CZTS has been performed using the spray pyrolysis method, including the emerging material CBaTS and CSrTS thin films. Initial screenings of candidates based on their abundance, toxicity and stability predictions as quaternary compounds resulted in seven potential candidates (Mn, Mg, Ni, Fe, Co, Ba and Sr).

After performing both thin film and solar cell device characterizations on various CXTS compounds, the following interpretations and design considerations can be concluded:

(a) The cation substitute must have d-orbitals to replace Zn and form a stable quaternary compound, as observed with the unsuccessful attempt to form Mg + CTS.

(b) The partially filled 3d-orbital of Fe, Ni, Co and Mn in this study increased the carrier concentration due to possible oxidation state changes and additional free carriers.

(c) The large ionic difference between the substitute and the host Cu and Sn may result in different quaternary crystal structures and optoelectronic properties. The change might also be a beneficial one, as observed in the sharp EQE for CBaTS.

(d) For substitutes that have similar structures between their secondary phases and quaternary phase, such as Ni + CTS, the fabrication needs to be done in a more controlled method to achieve a pure quaternary compound.

We found a notable photovoltaic response for CZTS, CMnTS, CBaTS, and CSrTS, and an ohmic response for Ni + CTS, CFeTS and CCoTS. This correlates with the large grain

size and sharper UV-Vis and EQE band edges in the first four compounds. On the other hand, the last 3 compounds without a PV effect do not form a quaternary compound, do not show any PL emission under 1 sun excitation, and/or have a small grain size and poor interface with Mo. This suggests that more specific synthesis parameters or post-synthesis treatments should be applied in the case of the Ni, Fe and Co substituent elements.

The photovoltaic response and the formation of a stable quaternary compound for CMnTS, CBaTS and CSrTS show the potential as emerging kesterite-inspired PV materials. The photoluminescence results also highlight the positive indication that CBaTS and CSrTS reduce defects near the band edges, but their deep defects and interface recombination have to be resolved. Finally, further optimization pathways should be considered to improve the photovoltaic response of these alternative emerging absorbers, such as finding the optimized stoichiometric ratio (e.g., the cations ratio) for each compound, optimizing the annealing parameters and/or different device configurations (e.g., different buffer layers).

## Conflicts of interest

There are no conflicts to declare.

## Acknowledgements

The authors acknowledge funding support from the CREATE Programme under the Campus for Research Excellence and Technological Enterprise (CREATE), which is supported by the National Research Foundation, Prime Minister's Office, Singapore; and Ministry of Education (MOE) Tier 2 Project (MOE2016-T2-1-030). Support by the Luxembourgish Fonds National de la Recherche FNR in the framework of the project CASK is acknowledged. The authors from IREC belong to the SEMS (Solar Energy Materials and Systems) Consolidated Research Group of the "Generalitat de Catalunya" (ref. 2017 SGR 862), and are grateful to the European Regional Development Funds (ERDF, FEDER Programa Competitivitat de Catalunya 2007–2013). M. G. acknowledges financial support from the Spanish Ministry of Science, Innovation and Universities within the Juan de la Cierva fellowship (IJC2018-038199-I).

## References

- 1 F. Oliva, L. Arqués, L. Acebo, M. Guc, Y. Sánchez, X. Alcobé, A. Pérez-Rodríguez, E. Saucedo and V. Izquierdo-Roca, *J. Mater. Chem. A*, 2017, **5**, 23863–23871.
- 2 W. Wang, M. T. Winkler, O. Gunawan, T. Gokmen, T. K. Todorov, Y. Zhu and D. B. Mitzi, *Adv. Energy Mater.*, 2014, **4**, 1301465.
- 3 D.-H. Son, S.-H. Kim, S.-Y. Kim, Y.-I. Kim, J.-H. Sim, S.-N. Park, D.-H. Jeon, D.-K. Hwang, S.-J. Sung and J.-K. Kang, *J. Mater. Chem. A*, 2019, **7**, 25279–25289.
- 4 Y. Gong, Y. Zhang, Q. Zhu, Y. Zhou, R. Qiu, C. Niu, W. Yan, W. Huang and H. Xin, *Energy Environ. Sci.*, 2021, **14**, 2369–2380.



5 Y. Gong, R. Qiu, C. Niu, J. Fu, E. Jedlicka, R. Giridharagopal, Q. Zhu, Y. Zhou, W. Yan, S. Yu, J. Jiang, S. Wu, D. S. Ginger, W. Huang and H. Xin, *Adv. Funct. Mater.*, 2021, **31**, 2101927.

6 W. Ki and H. W. Hillhouse, *Adv. Energy Mater.*, 2011, **1**, 732–735.

7 Y. Sun, P. Qiu, W. Yu, J. Li, H. Guo, L. Wu, H. Luo, R. Meng, Y. Zhang and S. Liu, *Adv. Mater.*, 2021, **33**, 2104330.

8 X. Xu, L. Guo, J. Zhou, B. Duan, D. Li, J. Shi, H. Wu, Y. Luo and Q. Meng, *Adv. Energy Mater.*, 2021, **11**, 2102298.

9 Y. Zhao, X. Zhao, D. Kou, W. Zhou, Z. Zhou, S. Yuan, Y. Qi, Z. Zheng and S. Wu, *ACS Appl. Mater. Interfaces*, 2021, **13**, 795–805.

10 Z. Su, G. Liang, P. Fan, J. Luo, Z. Zheng, Z. Xie, W. Wang, S. Chen, J. Hu, Y. Wei, C. Yan, J. Huang, X. Hao and F. Liu, *Adv. Mater.*, 2020, **32**, 2000121.

11 Y. Gong, Y. Zhang, E. Jedlicka, R. Giridharagopal, J. A. Clark, W. Yan, C. Niu, R. Qiu, J. Jiang, S. Yu, S. Wu, H. W. Hillhouse, D. S. Ginger, W. Huang and H. Xin, *Sci. China Mater.*, 2021, **64**, 52–60.

12 J. Li, Y. Huang, J. Huang, G. Liang, Y. Zhang, G. Rey, F. Guo, Z. Su, H. Zhu, L. Cai, K. Sun, Y. Sun, F. Liu, S. Chen, X. Hao, Y. Mai and M. A. Green, *Adv. Mater.*, 2020, **32**, 2005268.

13 S. K. Wallace, D. B. Mitzi and A. Walsh, *ACS Energy Lett.*, 2017, **2**, 776–779.

14 S. Hadke, M. Huang, C. Chen, Y. F. Tay, S. Chen, J. Tang and L. Wong, *Chem. Rev.*, 2021, DOI: 10.1021/acs.chemrev.1c00301.

15 K. Pal, P. Singh, A. Bhaduri and K. B. Thapa, *Sol. Energy Mater. Sol. Cells*, 2019, **196**, 138–156.

16 F. Liu, S. Wu, Y. Zhang, X. Hao and L. Ding, *Sci. Bulletin*, 2020, **65**, 698–701.

17 M. Ravindiran and C. Praveenkumar, *Renew. Sustain. Energy Rev.*, 2018, **94**, 317–329.

18 S. Giraldo, Z. Jehl, M. Placidi, V. Izquierdo-Roca, A. Pérez-Rodríguez and E. Saucedo, *Adv. Mater.*, 2019, **31**, 1806692.

19 M. Baid, A. Hashmi, B. Jain, A. K. Singh, M. A. B. H. Susan and M. Aleksandrova, *Opt. Quant. Electron.*, 2021, **53**, 656.

20 M. Kumar, A. Dubey, N. Adhikari, S. Venkatesan and Q. Qiao, *Energy Environ. Sci.*, 2015, **8**, 3134–3159.

21 M. Guc, S. Levchenko, I. V. Bodnar, V. Izquierdo-Roca, X. Fontane, L. V. Volkova, E. Arushanov and A. Pérez-Rodríguez, *Sci. Rep.*, 2016, **6**, 19414.

22 S. Levchenko, V. E. Tezlevan, E. Arushanov, S. Schorr and T. Unold, *Phys. Rev. B*, 2012, **86**(4), 045206.

23 A. Nagaoka, T. Masuda, S. Yasui, T. Taniyama and Y. Nose, *Jpn. J. Appl. Phys.*, 2018, **57**, 101201.

24 S. Podsiadlo, M. Bialogłowski, M. Fadaghi, W. Gebicki, C. Jastrzebski, E. Zero, D. Trzybinski and K. Wozniak, *Cryst. Res. Technol.*, 2015, **50**, 690–694.

25 K. Rudisch, A. Davydova, C. Platzer-Björkman and J. Scragg, *J. Appl. Phys.*, 2018, **123**, 161558.

26 A. Ritscher, M. Hoelzel and M. Lerch, *J. Solid State Chem.*, 2016, **238**, 68–73.

27 G. Rey, A. Redinger, J. Sendler, T. P. Weiss, M. Thevenin, M. Guennou, B. El Adib and S. Siebentritt, *Appl. Phys. Lett.*, 2014, **105**, 112106.

28 T. Gokmen, O. Gunawan, T. K. Todorov and D. B. Mitzi, *Appl. Phys. Lett.*, 2013, **103**, 103506.

29 S. Kim, J.-S. Park and A. Walsh, *ACS Energy Lett.*, 2018, **3**, 496–500.

30 Y. Gong, Y. Zhang, E. Jedlicka, R. Giridharagopal, J. A. Clark, W. Yan, C. Niu, R. Qiu, J. Jiang, S. Yu, S. Wu, H. W. Hillhouse, D. S. Ginger, W. Huang and H. Xin, *Sci. China Mater.*, 2020, **64**, 52–60.

31 J. S. Park, S. Kim, Z. Xie and A. Walsh, *Nat. Rev. Mater.*, 2018, **3**, 194–210.

32 S. Giraldo, Z. Jehl, M. Placidi, V. Izquierdo-Roca, A. Pérez-Rodríguez and E. Saucedo, *Adv. Mater.*, 2019, **31**, 1806692.

33 S. Kim, J. A. Márquez, T. Unold and A. Walsh, *Energy Environ. Sci.*, 2020, **13**, 1481–1491.

34 S. Kim, K. M. Kim, H. Tampo, H. Shibata and S. Niki, *Appl. Phys. Express*, 2016, **9**, 102301.

35 I. Kim, K. Kim, Y. Oh, K. Woo, G. Cao, S. Jeong and J. Moon, *Chem. Mater.*, 2014, **26**, 3957–3965.

36 A. Collard and H. Hillhouse, *Chem. Mater.*, 2016, **28**, 2067–2073.

37 K. Tsuji, T. Maeda and T. Wada, *Jpn. J. Appl. Phys.*, 2018, **57**, 08RC21.

38 S. Levchenko, M. Guc, C. Merschjann, G. Gurieva, S. Schorr, M. Lux-Steiner and E. Arushanov, *Phys. Status Solidi C*, 2013, **10**, 1079–1081.

39 L. Choubrac, M. Bär, X. Kozina, R. Felix, R. G. Wilks, G. Brammertz, S. Levchenko, L. Arzel, N. Barreau and S. Harel, *ACS Appl. Energy Mater.*, 2020, **3**, 5830–5839.

40 T. Schnabel, M. Seboui, A. Bauer, L. Choubrac, L. Arzel, S. Harel, N. Barreau and E. Ahlsweide, *RSC Adv.*, 2017, **7**, 40105–40110.

41 R. B. Wexler, G. S. Gautam and E. A. Carter, *J. Mater. Chem. A*, 2021, **9**, 9882–9897.

42 Z. Su, J. M. R. Tan, X. Li, X. Zeng, S. K. Batabyal and L. H. Wong, *Adv. Energy Mater.*, 2015, **5**(19), 1500682.

43 R. Sun, D. Zhuang, M. Zhao, Q. Gong, M. Scarpulla, Y. Wei, G. Ren and Y. Wu, *Sol. Energy Mater. Sol. Cells*, 2018, **174**, 494–498.

44 C. Yan, K. Sun, J. Huang, S. Johnston, F. Liu, B. P. Veettil, K. Sun, A. Pu, F. Zhou, J. A. Stride, M. A. Green and X. Hao, *ACS Energy Lett.*, 2017, **2**, 930–936.

45 S. H. Hadke, S. Levchenko, S. Lie, C. J. Hages, J. A. Márquez, T. Unold and L. H. Wong, *Adv. Energy Mater.*, 2018, **8**, 1802540.

46 S. Hadke, W. Chen, J. M. R. Tan, M. Guc, V. Izquierdo-Roca, G.-M. Rignanese, G. Hautier and L. H. Wong, *J. Mater. Chem. A*, 2019, **7**, 26927–26933.

47 S. Hadke, S. Levchenko, G. Sai Gautam, C. J. Hages, J. A. Márquez, V. Izquierdo-Roca, E. A. Carter, T. Unold and L. H. Wong, *Adv. Energy Mater.*, 2019, **9**, 1902509.

48 N. N. Greenwood and A. Earnshaw, *Chemistry of the Elements*, Elsevier, 2012.

49 R. Shannon, *Acta Crystallogr. A*, 1976, **32**, 751–767.

50 F. W. Clarke and H. S. Washington, *The Composition of the Earth's Crust*, US Government Printing Office, 1924.



51 G. B. Haxel, J. B. Hedrick and G. J. Orris, *Rare Earth Elements—Critical Resources for High Technology*, 2002, <https://pubs.usgs.gov/fs/2002/fs087-02>.

52 USGS, Commodity Statistics Information, <https://minerals.usgs.gov/minerals/pubs/commodity/>.

53 *Substance Listing - Letter A|Toxic Substance Portal|ATSDR*, 2021, <https://wwwn.cdc.gov/TSP/substances/SubstanceAZ.aspx>.

54 R. Chen and C. Persson, *J. Appl. Phys.*, 2017, **121**, 203104.

55 L. Weston and C. Stampfl, *Phys. Rev. Mater.*, 2018, **2**, 085407.

56 G. Zhong, K. Tse, Y. Zhang, X. Li, L. Huang, C. Yang, J. Zhu, Z. Zeng, Z. Zhang and X. Xiao, *Thin Solid Films*, 2016, **603**, 224–229.

57 G. Yang, X. Zhai, Y. Li, B. Yao, Z. Ding, R. Deng, H. Zhao, L. Zhang and Z. Zhang, *Mater. Lett.*, 2019, **242**, 58–61.

58 M. Wei, Q. Du, R. Wang, G. Jiang, W. Liu and C. Zhu, *Chem. Lett.*, 2014, **43**, 1149–1151.

59 C. L. Teske, *Z. Anorg. Allg. Chem.*, 1976, **419**, 67–76.

60 Z. Tong, J. Yuan, J. Chen, A. Wu, W. Huang, C. Han, Q. Cai, C. Ma, Y. Liu, L. Fang and Z. Liu, *Mater. Lett.*, 2019, **237**, 130–133.

61 T. Zhu, W. P. Huhn, G. C. Wessler, D. Shin, B. Saparov, D. B. Mitzi and V. Blum, *Chem. Mater.*, 2017, **29**, 7868–7879.

62 F. Hong, W. Lin, W. Meng and Y. Yan, *Phys. Chem. Chem. Phys.*, 2016, **18**, 4828–4834.

63 D. Shin, E. Ngaboyamahina, Y. Zhou, J. T. Glass and D. B. Mitzi, *J. Phys. Chem. Lett.*, 2016, **7**, 4554–4561.

64 Z. Xiao, W. Meng, J. V. Li and Y. Yan, *ACS Energy Lett.*, 2016, 29–35, DOI: 10.1021/acsenergylett.6b00577.

65 D. Shin, T. Zhu, X. Huang, O. Gunawan, V. Blum and D. B. Mitzi, *Adv. Mater.*, 2017, **29**(24), 1606945.

66 Z. Chen, K. Sun, Z. Su, F. Liu, D. Tang, H. Xiao, L. Shi, L. Jiang, X. Hao and Y. Lai, *ACS Appl. Energy Mater.*, 2018, **1**, 3420–3427.

67 T. Fries, Y. Shapira, F. Palacio, M. C. Morón, G. J. McIntyre, R. Kershaw, A. Wold and E. J. McNiff, *Phys. Rev. B*, 1997, **56**, 5424–5431.

68 L. Guen and W. S. Glaunsinger, *J. Solid State Chem.*, 1980, **35**, 10–21.

69 X. Liang, P. Guo, G. Wang, R. Deng, D. Pan and X. Wei, *RSC Adv.*, 2012, **2**, 5044.

70 L. Chen, H. Deng, J. Tao, H. Cao, L. Huang, L. Sun, P. Yang and J. Chu, *RSC Adv.*, 2015, **5**, 84295–84302.

71 G. P. Bernardini, D. Borrini, A. Caneschi, F. Di Benedetto, D. Gatteschi, S. Ristori and M. Romanelli, *Phys. Chem. Miner.*, 2000, **27**, 453–461.

72 V. S. Rusakov, N. I. Chistyakova, I. A. Burkovsky, A. M. Gapochka, T. L. Evstigneeva and S. Schorr, *J. Phys. Conf. Ser.*, 2010, **217**, 012038.

73 Y. Cui, R. Deng, G. Wang and D. Pan, *J. Mater. Chem.*, 2012, **22**, 23136–23140.

74 B. Murali, M. Madhuri and S. Krupanidhi, *Cryst. Growth Des.*, 2014, **14**, 3685–3691.

75 A. Ghosh, A. Biswas, R. Thangavel and G. Udayabhanu, *RSC Adv.*, 2016, **6**, 96025–96034.

76 F. Ozel, E. Aslan, B. Istanbullu, O. Akay and I. Hatay Patir, *Appl. Catal. B Environ.*, 2016, **198**, 67–73.

77 S. Rondiya, N. Wadnerkar, Y. Jadhav, S. Jadkar, S. Haram and M. Kabir, *Chem. Mater.*, 2017, **29**, 3133–3142.

78 C. L. Yang, Y. H. Chen, M. Lin, S. L. Wu, L. Li, W. C. Liu, X. S. Wu and F. M. Zhang, *Mater. Lett.*, 2016, **166**, 101–104.

79 Y. Cui, G. Wang and D. Pan, *J. Mater. Chem.*, 2012, **22**, 12471–12473.

80 M. Rouchdi, E. Salmani, N. Hassanain and A. Mzerd, *Opt. Quant. Electron.*, 2017, **49**(4), 1–12.

81 Q. Zhang, H. Deng, L. Chen, J. Tao, J. Yu, P. Yang and J. Chu, *Mater. Lett.*, 2017, **193**, 206–209.

82 D. B. Khadka and J. Kim, *J. Phys. Chem. C*, 2015, **119**, 1706–1713.

83 S. Chatterjee and A. J. Pal, *Sol. Energy Mater. Sol. Cells*, 2017, **160**, 233–240.

84 C. Dong, G. Y. Ashebir, J. Qi, J. Chen, Z. Wan, W. Chen and M. Wang, *Mater. Lett.*, 2018, **214**, 287–289.

85 A. Le Donne, S. Marchionna, M. Acciarri, F. Cernuschi and S. Binetti, *Sol. Energy*, 2017, **149**, 125–131.

86 R. R. Prabhakar, S. Zhenghua, Z. Xin, T. Baikie, L. S. Woei, S. Shukla, S. K. Batabyal, O. Gunawan and L. H. Wong, *Sol. Energy Mater. Sol. Cells*, 2016, **157**, 867–873.

87 J. Yu, H. Deng, Q. Zhang, J. Tao, L. Sun, P. Yang and J. Chu, *Mater. Lett.*, 2018, **233**, 111–114.

88 S. Marchionna, A. Le Donne, M. Merlini, S. Binetti, M. Acciarri and F. Cernuschi, *J. Alloys Compd.*, 2017, **693**, 95–102.

89 A. Crovetto, Z. Xing, M. Fischer, R. Nielsen, C. N. Savory, T. Rindzevicius, N. Stenger, D. O. Scanlon, I. Chorkendorff and P. C. K. Vesborg, *ACS Appl. Mater. Interfaces*, 2020, **12**, 50446–50454.

90 H. Xiao, Z. Chen, K. Sun, C. Yan, J. Xiao, L. Jiang, X. Hao, Y. Lai and F. Liu, *Thin Solid Films*, 2020, **697**, 137828.

91 J. Ge and Y. Yan, *J. Mater. Chem. C*, 2017, **5**, 6406–6419.

92 H. Guo, C. Ma, Z. Chen, X. Jia, Q. Cang, N. Yuan and J. Ding, *Sol. Energy*, 2019, **181**, 301–307.

93 T. H. Nguyen, W. Septina, S. Fujikawa, F. Jiang, T. Harada and S. Ikeda, *RSC Adv.*, 2015, **5**, 77565–77571.

94 X. Zeng, K. F. Tai, T. Zhang, C. W. J. Ho, X. Chen, A. Huan, T. C. Sum and L. H. Wong, *Sol. Energy Mater. Sol. Cells*, 2014, **124**, 55–60.

95 (a) T. Gokmen and O. Gunawan, Hall Measurement System with Rotary Magnet, *US Pat.*, 9041389, International Business Machines Corp., 2015; (b) Rotating magnetic Field Hall measurement system, *US Pat. App.* 14/682696, 14/748495, 2014.

96 O. Gunawan, Y. Virgus and K. F. Tai, *Appl. Phys. Lett.*, 2015, **106**, 062407.

97 J. J. Scragg, T. Ericson, T. Kubart, M. Edoff and C. Platzer-Björkman, *Chem. Mater.*, 2011, **23**, 4625–4633.

98 A. C. Lokhande, R. B. V. Chalapathy, M. He, E. Jo, M. Gang, S. A. Pawar, C. D. Lokhande and J. H. Kim, *Sol. Energy Mater. Sol. Cells*, 2016, **153**, 84–107.

99 W. Li, J. Chen, C. Yan and X. Hao, *J. Alloys Compd.*, 2015, **632**, 178–184.

100 X. Zeng, S. S. Pramana, S. K. Batabyal, S. G. Mhaisalkar, X. Chen and K. B. Jinesh, *Phys. Chem. Chem. Phys.*, 2013, **15**, 6763–6768.



101 C. Wang, S. Chen, J.-H. Yang, L. Lang, H.-J. Xiang, X.-G. Gong, A. Walsh and S.-H. Wei, *Chem. Mater.*, 2014, **26**, 3411–3417.

102 L. Kaupmees, M. Altosaar, O. Volobujeva, T. Raadik, M. Grossberg, M. Danilson, E. Mellikov and P. Barvinschi, *Adv. Mater. Sci. Eng.*, 2012, **2012**, 11.

103 K.-L. Huang, C.-H. Huang, W.-T. Lin, Y.-S. Fu and T.-F. Guo, *J. Alloys Compd.*, 2015, **646**, 1015–1022.

104 Y. Zhu, Y. Liu, G. Ren, X. Tan, M. Yu, Y. H. Lin, C. W. Nan, A. Marcelli, T. Hu and W. Xu, *Inorg. Chem.*, 2018, **57**, 6051–6056.

105 Q. Zhang, H. Deng, L. Chen, L. Yu, J. Tao, L. Sun, P. Yang and J. Chu, *J. Alloys Compd.*, 2017, **695**, 482–488.

106 K.-L. Ou, J.-C. Fan, J.-K. Chen, C.-C. Huang, L.-Y. Chen, J.-H. Ho and J.-Y. Chang, *J. Mater. Chem.*, 2012, **22**, 14667–14673.

107 M. S. Faber, M. A. Lukowski, Q. Ding, N. S. Kaiser and S. Jin, *J. Phys. Chem. C Nanomater. Interfaces*, 2014, **118**, 21347–21356.

108 X. Fontané, V. Izquierdo-Roca, E. Saucedo, S. Schorr, V. O. Yukhymchuk, M. Y. Valakh, A. Pérez-Rodríguez and J. R. Morante, *J. Alloys Compd.*, 2012, **539**, 190–194.

109 L. Chen, H. Deng, J. Tao, W. Zhou, L. Sun, F. Yue, P. Yang and J. Chu, *J. Alloys Compd.*, 2015, **640**, 23–28.

110 C. Rincón, M. Quintero, E. Moreno, C. Power, E. Quintero, J. Henao, M. Macías, G. Delgado, R. Tovar and M. Morocoima, *Solid State Commun.*, 2011, **151**, 947–951.

111 M. Himmrich and H. Haeuseler, *Spectrochim. Acta Part A Mol. Spectrosc.*, 1991, **47**, 933–942.

112 J. Zhong, Q. Wang and W. Cai, *Mater. Lett.*, 2015, **150**, 69–72.

113 S. Schorr, G. Gurieva, M. Guc, M. Dimitrieva, A. Pérez-Rodríguez, V. Izquierdo-Roca, C. S. Schnohr, J. Kim, W. Jo and J. M. Merino, *J. Phys. Energy*, 2019, **2**, 012002.

114 J. Ge, P. Koirala, C. R. Grice, P. J. Roland, Y. Yu, X. Tan, R. J. Ellingson, R. W. Collins and Y. Yan, *Adv. Energy Mater.*, 2016, 1601803, DOI: 10.1002/aenm.201601803.

115 C. Persson, *J. Appl. Phys.*, 2010, **107**, 053710.

116 A. Ghosh, R. Thangavel and M. Rajagopalan, *Energy Environ. Focus*, 2014, **3**, 142–151.

117 S. Palaz, H. Unver, G. Ugur, A. M. Mamedov and E. Ozbay, *IOP Conf. Ser. Mater. Sci. Eng.*, 2017, **175**, 012014.

118 T. Fukushima, K. Yamauchi and S. Picozzi, *Phys. Rev. B*, 2010, **82**.

119 T.-X. Wang, Y.-G. Li, H.-R. Liu, H. Li and S.-X. Chen, *Mater. Lett.*, 2014, **124**, 148–150.

120 A. Kamble, K. Mokurala, A. Gupta, S. Mallick and P. Bhargava, *Mater. Lett.*, 2014, **137**, 440–443.

121 F. Ozel, *J. Alloys Compd.*, 2016, **657**, 157–162.

122 S. Sarkar, B. Das, P. R. Midya, G. C. Das and K. K. Chattopadhyay, *Mater. Lett.*, 2015, **152**, 155–158.

123 S. Chen, A. Walsh, X.-G. Gong and S.-H. Wei, *Adv. Mater.*, 2013, **25**, 1522–1539.

124 D. Shin, B. Saparov and D. B. Mitzi, *Adv. Energy Mater.*, 2017, **7**, 1602366.

125 A. Murphy, *Sol. Energy Mater. Sol. Cells*, 2007, **91**, 1326–1337.

126 A. Nagoya, R. Asahi and G. Kresse, *J. Phys. Condens. Matter*, 2011, **23**, 404203.

127 H. Katagiri, K. Jimbo, W. S. Maw, K. Oishi, M. Yamazaki, H. Araki and A. Takeuchi, *Thin Solid Films*, 2009, **517**, 2455–2460.

128 D. B. Mitzi, O. Gunawan, T. K. Todorov, K. Wang and S. Guha, *Sol. Energy Mater. Sol. Cells*, 2011, **95**, 1421–1436.

129 P. Baláž, M. Baláž, M. J. Sayagués, A. Eliyas, N. G. Kostova, M. Kaňuchová, E. Dutková and A. Zorkovská, *Crystals*, 2017, **7**, 367.

130 P. A. Fernandes, P. M. P. Salomé and A. F. d. Cunha, *J. Phys. D: Appl. Phys.*, 2010, **43**, 215403.

131 M. Krishnaiah, R. K. Mishra, S. G. Seo, S. H. Jin and J. T. Park, *Ceram. Int.*, 2019, **45**, 12399–12405.

132 K. F. Tai, O. Gunawan, M. Kuwahara, S. Chen, S. G. Mhaisalkar, C. H. A. Huan and D. B. Mitzi, *Adv. Energy Mater.*, 2016, **6**(3), 1501609.

133 J. Dziewior and W. Schmid, *Appl. Phys. Lett.*, 1977, **31**, 346–348.

134 S. Lie, J. M. Rui Tan, W. Li, S. W. Leow, Y. F. Tay, D. M. Bishop, O. Gunawan and L. H. Wong, *J. Mater. Chem. A*, 2018, **6**, 1540–1550.

135 C. E. Housecroft and A. G. Sharpe, *Inorganic Chemistry*, Pearson Prentice Hall, 2005.

136 S. Lie, S. W. Leow, D. M. Bishop, M. Guc, V. Izquierdo-Roca, O. Gunawan and L. H. Wong, *ACS Appl. Mater. Interfaces*, 2019, **11**, 25824–25832.

137 G.-X. Liang, Y.-D. Luo, J.-G. Hu, X.-Y. Chen, Y. Zeng, Z.-H. Su, J.-T. Luo and P. Fan, *Surf. Coat. Technol.*, 2019, **358**, 762–764.

138 Z. Su, G. Liang, P. Fan, J. Luo, Z. Zheng, Z. Xie, W. Wang, S. Chen, J. Hu and Y. Wei, *Adv. Mater.*, 2020, **32**, 2000121.

139 S. Lie, W. Li, S. W. Leow, D. M. Bishop, O. Gunawan and L. Helena Wong, *Sol. RRL*, 2020, **4**, 1900521.

140 X. Meng, H. Deng, J. He, L. Sun, P. Yang and J. Chu, *Mater. Lett.*, 2015, **151**, 61–63.

141 A. Ghosh, D. K. Chaudhary, A. Biswas, R. Thangavel and G. Udayabhanu, *RSC Adv.*, 2016, **6**, 115204–115212.

142 D. Shin, B. Saparov, T. Zhu, W. P. Huhn, V. Blum and D. B. Mitzi, *Chem. Mater.*, 2016, **28**, 4771–4780.

143 G. Rey, G. Larramona, S. Bourdais, C. Choné, B. Delatouche, A. Jacob, G. Dennler and S. Siebentritt, *Sol. Energy Mater. Sol. Cells*, 2018, **179**, 142–151.

144 M. Kumar, A. Dubey, N. Adhikari, S. Venkatesan and Q. Qiao, *Energy Environ. Sci.*, 2015, **8**, 3134–3159.

145 S. Siebentritt, T. P. Weiss, M. Sood, M. H. Wolter, A. Lomuscio and O. Ramirez, *J. Phys. Mater.*, 2021, **4**, 042010.

146 G. Rey, T. Weiss, J. Sendler, A. Finger, C. Spindler, F. Werner, M. Melchiorre, M. Hala, M. Guennou and S. Siebentritt, *Sol. Energy Mater. Sol. Cells*, 2016, **151**, 131–138.

147 S. Levcenko, V. Tezlevan, E. Arushanov, S. Schorr and T. Unold, *Phys. Rev. B*, 2012, **86**, 045206.

148 M. A. Green, *Prog. Photovoltaics Res. Appl.*, 2012, **20**, 472–476.



149 P. Caprioglio, M. Stolterfoht, C. M. Wolff, T. Unold, B. Rech, S. Albrecht and D. Neher, *Adv. Energy Mater.*, 2019, **9**, 1901631.

150 M. Sood, A. Urbaniak, C. Kameni Boumenou, T. P. Weiss, H. Elanzeery, F. Babbe, F. Werner, M. Melchiorre and S. Siebentritt, *Prog. Photovoltaics Res. Appl.*, 2022, **30**(3), 263–275.

151 M. Sood, A. Urbaniak, C. K. Boumenou, T. Weiss, H. Elanzeery, F. Babbe, F. Werner, M. Melchiorre and S. Siebentritt, arXiv:2103.15616, 2021.

